

Energy-resolved spin correlation measurements: Decoding transverse spin dynamics in weakly interacting Fermi gases

J. Huang^{✉*} and J. E. Thomas^{✉†}

Department of Physics, North Carolina State University, Raleigh, North Carolina 27695, USA

 (Received 13 September 2023; revised 1 December 2023; accepted 28 March 2024; published 10 April 2024)

We study transverse spin dynamics on a microscopic level by measuring energy-resolved spin correlations in weakly interacting Fermi gases (WIFGs). The trapped cloud behaves as a many-body spin lattice in energy space with effective long-range interactions, simulating a collective Heisenberg model. We observe the flow of correlations in energy space in this quasi-continuous system, revealing the connection between the evolution of the magnetization and the localization or spread of correlations. This work highlights energy-space correlation as an observable in quantum phase transition studies of WIFGs, decoding system features that are hidden in macroscopic measurements.

DOI: [10.1103/PhysRevA.109.L041301](https://doi.org/10.1103/PhysRevA.109.L041301)

Collective spin dynamics plays a central role in spin-lattice models, such as Heisenberg models of quantum magnetism [1], Anderson pseudospin models of superconductivity [2], and Richardson-Gaudin models of pairing [3]. These models have been simulated in discrete systems, including ion traps [4–6], quantum gas microscopes [7], and cavity-QED experiments [8], which achieve single-site resolution. In contrast, weakly interacting Fermi gases (WIFGs) provide a powerful many-body platform for realizing spin-lattice models in a quasi-continuous system. In the nearly collisionless regime, the energy states of the individual atoms are preserved over experimental time scales, creating a long-lived synthetic lattice [9] in energy space that is not achievable in a strongly interacting regime. This energy lattice simulates collective Heisenberg Hamiltonians with tunable long-range interactions [10–17] and adjustable anisotropy [18].

In this work, we demonstrate measurements of energy-resolved spin correlations, which provide a physically intuitive picture of the transverse spin dynamics in an energy-space spin lattice. This method enables a microscopic look into the signatures of quantum phase transitions and the origins of the macroscopic properties, such as magnetization. In a many-body spin lattice with a collective Heisenberg Hamiltonian, the interplay between the site-dependent energy and site-to-site interactions leads to a transition to a spin-locked state as the interaction strength is increased, producing a large total transverse spin. This transition has been observed in a WIFG of ^{40}K [16], using the total transverse magnetization as the order parameter. More insight into the spin-locking transition is provided by our energy-resolved measurements, which illustrate the emergence of strong correlations between transverse spin components in localized low-energy and high-energy subgroups and the spread of these

correlations throughout the energy lattice as interaction strength increases.

The observation of energy-resolved transverse correlation is implemented in a degenerate Fermi gas, consisting of 6.2×10^4 ^6Li atoms. The cloud is confined in an optical trap and cooled to temperature $T = 0.21 T_F$, where Fermi temperature $T_F \approx 0.73 \mu\text{K}$. The ratio between radial and axial trap frequencies is $\omega_r/\omega_x \approx 27$, allowing a quasi-one-dimensional (quasi-1D) approximation for modeling. A superposition of the two lowest hyperfine-Zeeman states, which are denoted by $|\uparrow_z\rangle$ and $|\downarrow_z\rangle$, is prepared by an rf pulse at the beginning of each experimental cycle.

The collision rate is controlled to be negligible during a single cycle by tuning the bias magnetic field B to provide a sufficiently small scattering length $a(B)$. Therefore, in such a weakly interacting regime, the energy and the energy state of each particle are conserved, allowing us to simulate the system as a 1D lattice in energy space. Each lattice site i represents the i th harmonic oscillator state along the axial direction of the sample, with an energy $E_i = (n_i + 1/2) \hbar\omega_x$ and dimensionless collective spin vector $\vec{s}(E_i) \equiv \vec{s}_i$. Hence, this synthetic lattice can be described by a Heisenberg Hamiltonian [12]:

$$\frac{H(a)}{\hbar} = \sum_{i,j \neq i} g_{ij}(a) \vec{s}_i \cdot \vec{s}_j + \sum_i \Omega' E_i s_{zi}. \quad (1)$$

The first term represents the effective long-range interactions between energy lattice site i and j due to the overlap of probability densities in real space for the energy states i and j . $g_{ij}(a)$ is the coupling parameter, scaling linearly with scattering length a . The average of $g_{ij}(a)$ for all ij pairs is denoted by $\bar{g}(a)$.

The second term arises from the magnetic field variation along the axial direction of the cloud, resulting in an effective spin-dependent harmonic potential and corresponding site-dependent detuning rate $\Omega' = -\delta\omega_x/(\hbar\omega_x)$. The statistical standard deviation of $\Omega' E_i$, denoted by $\sigma_{\Omega'}$, determines the spread in the spin-precession rate, $\sigma_{\Omega'} \approx 1.4\text{Hz}$ in our system.

*Corresponding author: jhuang39@ncsu.edu

†Corresponding author: jethoma7@ncsu.edu

The ratio of these two terms in Eq. (1) determines the behavior of the system during evolution. For this reason, we define the dimensionless interaction strength $\zeta \equiv \bar{g}(a)/(\sqrt{2}\sigma_{\Omega_z})$. Here, larger ζ represents a stronger mean-field interaction, and for small ζ , the system is dominated by the spread in Zeeman precession.

To predict the dynamics of the system with the Hamiltonian Eq. (1), a quasi-classical spin model is adopted. In the simulation, a mean-field approximation is applied, and the classical collective spin vectors are obtained by neglecting quantum correlations in the Heisenberg equations: $\dot{\vec{s}}_i = [\sum_{j \neq i} g_{ij}(a)\vec{s}_j + \Omega'E_i\hat{e}_z] \times \vec{s}_i$ [12,19]. The components of collective spin vectors for different energy groups $s_\sigma(E_i)$ are obtained by numerical integration. This equation of motion describes the evolution of spin vectors in the Bloch resonant frame, which rotates at the instantaneous hyperfine resonant frequency for the particles in the lowest energy site: $E_i = 0$.

To observe the transverse component of the spin vector, a Ramsey sequence is applied. Starting from an initially z -polarized state, the first excitation $(\frac{\pi}{2})_y$ rf pulse produces an x -polarized sample. After that, the system is allowed to evolve for a period τ at the scattering length a of interest. Then, a second $(\frac{\pi}{2})_y$ rf pulse is applied to collectively rotate the spin vectors about the y axis, projecting the x component onto the measurement z axis, ideally. Immediately after the last rf pulse, spin states $|\uparrow_z\rangle$ and $|\downarrow_z\rangle$ are imaged. In reality, as discussed below, $s_z(x) = [n_\uparrow(x) - n_\downarrow(x)]/2 \equiv s^{\text{meas}}(x)$ measures a combination of transverse components of the spin vector in the Bloch resonant frame, \tilde{s}_x and \tilde{s}_y , just prior to imaging.

In this quasi-continuous spin system, which contains a large number of atoms with closely spaced energy levels, the spin profiles in real space and in energy space are related by [20]

$$s^{\text{meas}}(x) = \frac{1}{\pi} \int dE |\phi_E(x)|^2 s^{\text{meas}}(E). \quad (2)$$

$|\phi_E(x)|^2$ is the probability density which is evaluated using a WKB approximation. Using Abel inversion, Eq. (2) yields the energy-resolved spin density $\{s^{\text{meas}}(E)|E \in [0, E_F]\}$ from measurements in real space $\{s^{\text{meas}}(x)|x \in [-\sigma_{F_x}, \sigma_{F_x}]\}$ [20,21]. E_F is the effective Fermi energy and σ_{F_x} is the fitted Thomas-Fermi width of the cloud. In the data analysis, we use an energy bin width of $\Delta E = E_F/50$ limited by imaging resolution and the mapping algorithm.

During the experimental cycle, magnetic field fluctuation, at even 10^{-4} G level, causes imperfectly controlled rf detuning and subsequent phase φ accumulation, changing the relative contribution of the x and y components of spin vectors in the measurement, $s^{\text{meas}} = \cos(\varphi)\tilde{s}_x + \sin(\varphi)\tilde{s}_y$. With a broad spread $\varphi \in [0, 2\pi]$, a multishot average $\langle s^{\text{meas}} \rangle$ tends to vanish. As the φ distribution for each data set is usually irreproducible, the contribution of the x and y components in $\langle s^{\text{meas}} \rangle$ cannot be controlled efficiently and reliably, even with data selection [20].

In the analysis of s^{meas} correlations presented in this work, this problem is circumvented. The correlation between

measured operators with energy E_i and E_j has the form [20]

$$\begin{aligned} C_{ij}^\perp \equiv \langle s_i^{\text{meas}} s_j^{\text{meas}} \rangle &= \frac{1}{2} \langle \tilde{s}_{xi} \tilde{s}_{xj} + \tilde{s}_{yi} \tilde{s}_{yj} \rangle \\ &+ \frac{1}{2} \langle \cos(2\varphi) \rangle \langle \tilde{s}_{xi} \tilde{s}_{xj} - \tilde{s}_{yi} \tilde{s}_{yj} \rangle \\ &- \frac{1}{2} \langle \sin(2\varphi) \rangle \langle \tilde{s}_{xi} \tilde{s}_{yj} + \tilde{s}_{yi} \tilde{s}_{xj} \rangle, \quad (3) \end{aligned}$$

where $\langle \dots \rangle$ denotes an average over multishots, and $\tilde{s}_{\sigma i}$ is the σ component of spin vector in the Bloch frame before the last $(\frac{\pi}{2})_y$ pulse. In the data analysis, a data group is selected with a specific phase distribution [20] to enforce $\langle \cos(2\varphi) \rangle = \langle \sin(2\varphi) \rangle = 0$, estimated using the quasi-classical spin model. This method ensures that the correlation obtained by averaging the selected data is $C_{ij}^\perp = \frac{1}{2} \langle \tilde{s}_{xi} \tilde{s}_{xj} + \tilde{s}_{yi} \tilde{s}_{yj} \rangle$, without making assumptions about the φ distribution for the whole data set.

In contrast, the longitudinal spin vectors and its correlation, $\langle \tilde{s}_{zi} \rangle$ and $\langle \tilde{s}_{zi} \tilde{s}_{zj} \rangle$, can be measured easily without data selection, as this measurement does not require the last $(\frac{\pi}{2})_y$ rf pulse, and therefore is insensitive to the rf detuning. We have conducted ensemble-averaged \tilde{s}_z measurement and found that $(\langle \tilde{s}_{zi} \tilde{s}_{zj} \rangle - \langle \tilde{s}_{zi} \rangle \langle \tilde{s}_{zj} \rangle) / (N_i N_j / 4)$ has a value of $\sim 5 \times 10^{-3}$, which is comparable to spin projection noise, indicating the system is not quantum correlated. In addition, as our previous single-shot measurements showed, this large spin system can be well explained by the quasi-classical model [19]. Therefore, this system is expected to evolve classically, where the classical correlation C_{ij}^\perp is of interest. By construction, C_{ij}^\perp also detects quantum correlations when they are present.

To study the correlation between one pair of particles with energies E_i and E_j , C_{ij}^\perp is normalized by atom numbers in the i th and j th energy partitions, N_i and N_j . The normalized transverse correlation is defined as $c_{ij}^\perp \equiv C_{ij}^\perp / (\frac{N_i N_j}{4})$. Then, by construction from Eq. (3), $c_{ij}^\perp \in [-\frac{1}{2}, \frac{1}{2}]$. In this work, it is observed that the normalized transverse correlation evolves in qualitatively distinct ways as the interaction strength ζ increases.

Figure 1 illustrates the different behaviors of c_{ij}^\perp at $\zeta = 1.2$ [Figs. 1(a)–1(c)] and $\zeta = 1.8$ [Figs. 1(d)–1(f)]. At early time, for both interaction strengths, the spins are x -polarized and the transverse spin components are mostly self-correlated, and their c_{ij}^\perp have very similar distributions in energy space as shown in Figs. 1(a) and 1(d). As time evolves, in the system with smaller interaction strength [Figs. 1(b) and 1(c)], the single particle correlation tends to be localized between multiple specific energy subgroups. In contrast, for the case with stronger interaction [Figs. 1(e) and 1(f)], the correlation tends to become more uniform across all pairs of energy groups at a later time. This distinct behavior of microscopic correlations reveals the source of the phase transition that the system undergoes.

In addition to visualizing the distribution of highly correlated regions in the energy lattice using surface plots (Fig. 1), the energy-resolved transverse correlation measurement directly yields the macroscopic transverse magnetization, which undergoes a phase transition as interaction strengths increase. The system magnetization is related to the ensemble-averaged correlation functions. The square of total transverse magnetization $\mathcal{M}_\perp^2 = S_x^2 + S_y^2$ is the double summation of

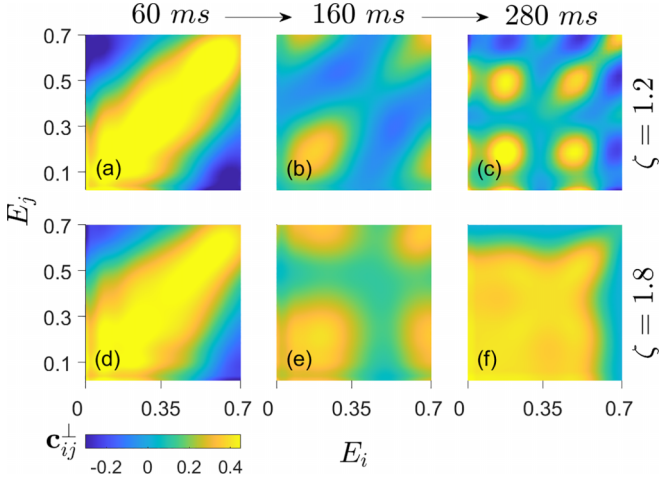


FIG. 1. Correlation function \mathbf{c}_{ij}^{\perp} , ensemble-averaged over 30 shots with a selected φ distribution, at different evolution times with interaction strength $\zeta = 1.2$ (a)–(c) and $\zeta = 1.8$ (d)–(f). E_i and E_j are in units of effective Fermi energy E_F . Only the lowest 70% of energy bins are adopted in data analysis as higher energy groups contain very few particles. The \mathbf{c}_{ij}^{\perp} values shown here and in Figs. 2(c)–2(e) and 2(h)–2(j) are amplified by dividing by an energy-dependent attenuation coefficient $\Gamma(E_i)$ arising from the finite energy resolution ($\lesssim 0.08\sqrt{E_i}$) to restore the amplitudes to their correct values [20].

the transverse correlation in energy space: $\frac{1}{2}\mathcal{M}_{\perp}^2 = \sum_{i,j} C_{ij}^{\perp}$. In this way, $\frac{1}{2}\mathcal{M}_{\perp}^2$ data presented in this work are calculated using our measured C_{ij}^{\perp} . However, the macroscopic magnetization does not fully represent the structure of the correlations across the energy-space landscape.

The C_{ij}^{\perp} measurement opens different ways to observe the microscopic spin dynamics of the system in energy space. One method to describe the microscopic information is to quantify the extent of the correlations by determining the magnitude of the correlation gradient near the point of maximum correlation \mathcal{D}_m . To calculate \mathcal{D}_m from the correlation matrix \mathbf{c}_{ij}^{\perp} , first, we find the energy partition $E_i = E_m$ where the center of the highest correlated region is located. Then, we calculate the absolute values of the gradient for the transverse spin correlation between this energy partition and all other partitions, \mathbf{c}_{mj}^{\perp} . Finally, \mathcal{D}_m is defined as the average magnitude of the gradient of \mathbf{c}_{mj}^{\perp} for all energy partitions $j \in [1, j_{\max}]$ for the fixed m :

$$\mathcal{D}_m \equiv \frac{1}{j_{\max}} \sum_{j=1}^{j_{\max}} |\nabla \mathbf{c}_{mj}^{\perp}|, \quad (4)$$

where j_{\max} is the number of total energy groups adopted in data analysis [20]. Therefore, \mathcal{D}_m measures the maximum magnitude of the gradient for normalized correlations between transverse spin vectors in one energy partition and in all other partitions. A large \mathcal{D}_m value indicates that high correlations cluster around specific energy-group pairs E_m and some of E_j . A small \mathcal{D}_m means that the high correlation region is spread evenly across most lattice site pairs in energy space.

The time evolution of \mathcal{M}_{\perp}^2 and \mathcal{D}_m at different interaction strengths is shown along with corresponding microscopic

transverse correlation plots in Fig. 2. In this figure, panels in the left half [Figs. 2(a)–2(e)] for small interaction strength ζ and panels in the right half [Figs. 2(f)–2(j)] for large interaction strength demonstrate two distinct behaviors as time evolves. As each sample is initially x -polarized, at $\tau = 0$ ms the transverse magnetizations $\frac{1}{2}\mathcal{M}_{\perp}^2$ are maximum and the transverse correlation is strong between most energy groups. For relatively short evolution time ($\tau < 60$ ms), the site-dependent Zeeman tuning [second term in Eq. (1)] dominates the system behavior for all the scattering lengths studied in this work, causing the systems to behave similarly: the spin vectors spread out in the transverse plane, making $\frac{1}{2}\mathcal{M}_{\perp}^2$ decrease and \mathcal{D}_m increase initially. The behaviors of systems with small and large interaction strengths become distinct over extended periods of evolution. A system with small interaction strength ($\zeta = 0, 0.6, 1.2$) tends to demagnetize as time evolves: $\frac{1}{2}\mathcal{M}_{\perp}^2(t \rightarrow \infty)$ asymptotes to a small value [Fig. 2(a)]. The normalized transverse correlation in such a system acts similarly to the example in the top row of Fig. 1: the largest correlations $|\mathbf{c}_{ij}^{\perp}|$ (either positive or negative) arise between certain localized energy groups, either forming thin stripes or forming islands, as shown in Figs. 2(c)–2(e). The corresponding maximum correlation gradient at these interaction strengths increases over time [Fig. 2(b)], in agreement with the features of surface plots [Figs. 2(c)–2(e)]. In contrast, for stronger interactions ($\zeta \geq 1.8$), $\frac{1}{2}\mathcal{M}_{\perp}^2(t \rightarrow \infty)$ oscillates relative to a larger static level as ζ increases [Fig. 2(f)]. In such cases, Figs. 2(h)–2(j) suggest that the high correlation domain tends to extend over all pairs of energy lattice sites, as opposed to the trend in Figs. 2(c)–2(e). The measurement of \mathcal{D}_m illustrates this trend in a quantitative way: \mathbf{c}_{ij}^{\perp} has a persistent low correlation gradient [Fig. 2(g)], corresponding to an extended correlation region.

Furthermore, even when \mathcal{M}_{\perp}^2 has the same value at two different times, by comparing the corresponding correlation plots, it is observed that the strongly correlated region in energy space can have completely different distributions. For example, for $\zeta = 1.8$ (the lightest green data) in Fig. 2(f), $\mathcal{M}_{\perp}^2(80 \text{ ms}) = \mathcal{M}_{\perp}^2(200 \text{ ms})$, but the corresponding \mathbf{c}_{ij}^{\perp} [Fig. 2(h)] shows different features for these two times: at 80 ms, the transverse spin vectors are strongly correlated mainly between low-energy groups, and in contrast, at 200 ms, the high transverse correlation domain has extended to energy partition pairs that are further apart. Similarly, for $\zeta = 1.2$ (the darkest blue data) in Fig. 2(a), $\mathcal{M}_{\perp}^2(200 \text{ ms}) = \mathcal{M}_{\perp}^2(280 \text{ ms})$, but Figs. 2(e) and 1(c) show different distributions of \mathbf{c}_{ij}^{\perp} . These different structures observed in correlation plots are very well represented by corresponding high and low values of \mathcal{D}_m for these cases. Therefore, the observations of energy-resolved transverse correlation provide different probes to characterize the spin dynamics more deeply than simply measuring macroscopic quantities.

From the measured energy-space correlation function \mathbf{c}_{ij}^{\perp} , we conclude that a system with a more localized transverse correlation between multiple specific energy-group pairs tends to be demagnetized as time evolves [Fig. 2(a)]. In contrast, a system with the transverse correlation spread over most energy lattice site pairs at a long evolution time maintains the high initial magnetization [Fig. 2(b)]. These transitions in the magnetization with increasing interaction

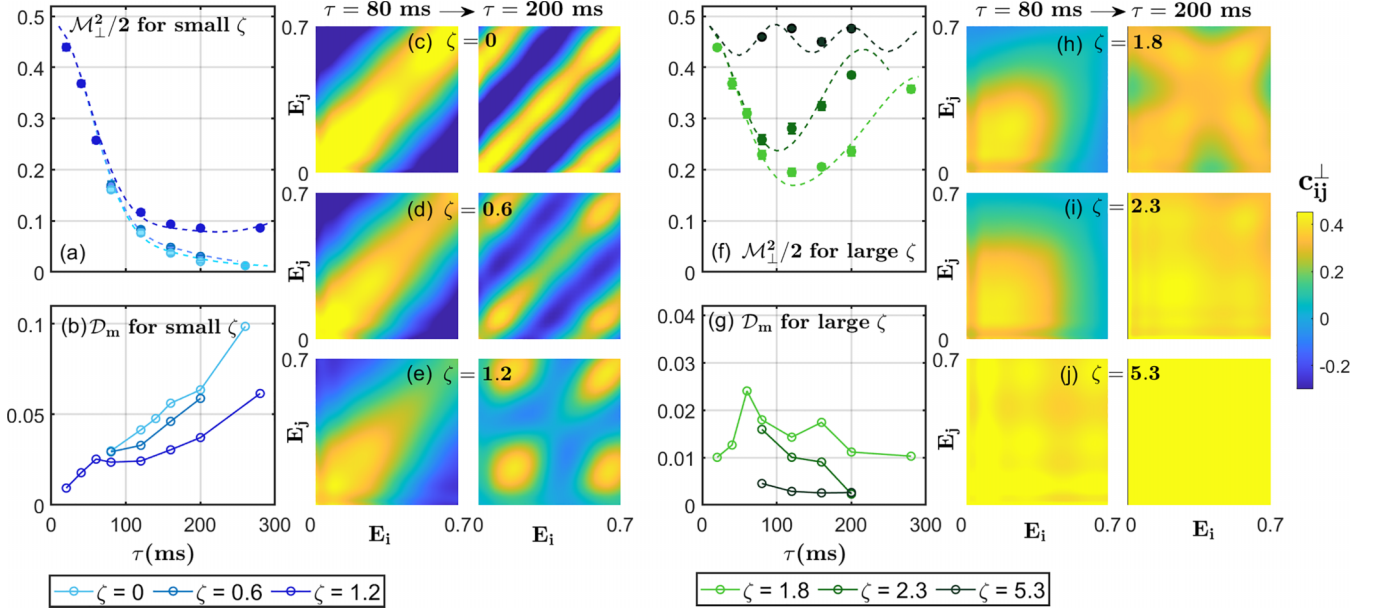


FIG. 2. Time-dependent transverse magnetization ($\frac{1}{2}\mathcal{M}_\perp^2$) and correlation gradient (\mathcal{D}_m) at different interaction strengths ζ , along with corresponding c_{ij}^\perp correlation plots. Solid circles in (a) and (f) are $\frac{1}{2}\mathcal{M}_\perp^2$ obtained by ensemble averaging over multiple shots with the desired φ distribution. Darker blue or green corresponds to the cases with stronger interaction. A detailed description of data selection and error bar calculation is in Supplemental Material [20]. Dashed lines are predictions from the quasi-classical spin model [12,19]. Hollow circles in (b) and (g) are correlation gradient \mathcal{D}_m extracted from normalized correlation c_{ij}^\perp data at corresponding interaction strength and evolution time. Note that the vertical scale in (g) is expanded to show the details. Correlation plots (c)–(e) and (h)–(j) show c_{ij}^\perp at $\tau = 80$ ms (left of each pair) and 200 ms (right of each pair). (c) $\zeta = 0$ ($a = 0a_0$), (d) $\zeta = 0.6$ ($a = 2.62a_0$), (e) $\zeta = 1.2$ ($a = 5.19a_0$), (h) $\zeta = 1.8$ ($a = 8.05a_0$), (i) $\zeta = 2.3$ ($a = 10.54a_0$), (j) $\zeta = 5.3$ ($a = 23.86a_0$).

strength are shown in Fig. 3 for four evolution times. Blue circles are \mathcal{M}_\perp^2 obtained directly from the double sum of the correlation function as described above. Predictions of \mathcal{M}_\perp^2 (red curves) are obtained using the quasi-classical model. We find that, as the interaction strength increases, the transverse magnetization surges, simulating the transition from a paramagnetic phase to a ferromagnetic phase. Figures 2(c)–2(e) and 2(h)–2(j) show how the corresponding spin correlations change from localized to global across this transition.

In summary, we have developed energy-space spin correlation measurement as a method for characterizing the spin dynamics of quasi-continuous systems, which simulate a synthetic lattice of spins pinned in energy space. This method

enables a full microscopic view of how correlations develop between the extensive subsets of spins in energy space, associating the evolution of the macroscopic properties with the local correlation behavior. Utilizing this idea, we connect the spread and localization of correlations to the system magnetization and demagnetization by observing the correlation distribution as a function of time and interaction strength.

The observables developed in this work are broadly applicable in weakly interacting quantum gases. In these systems, long-range interactions between lattice sites in energy space can be engineered to simulate a wide variety of model Hamiltonians. For example, tunable spatial asymmetry can be introduced into the coupling constant by creating

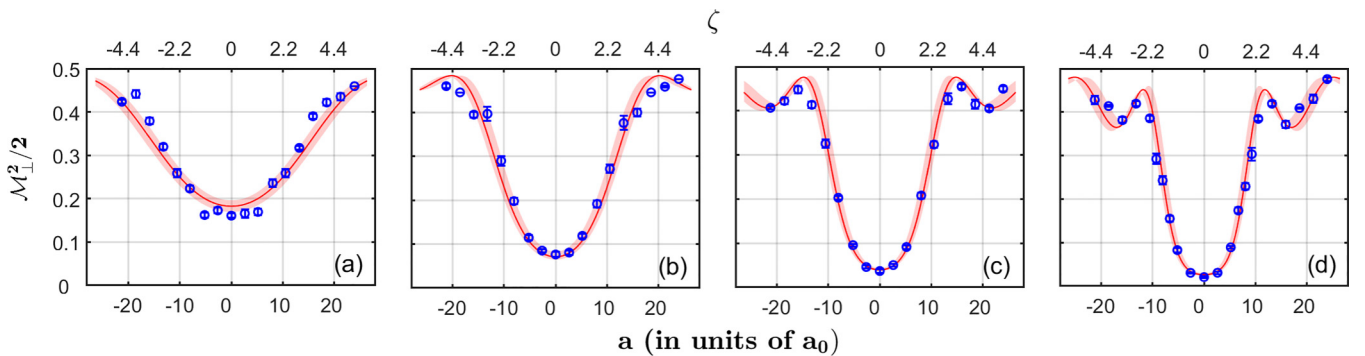


FIG. 3. Observing the emergence of spin locking by measuring $\frac{1}{2}\mathcal{M}_\perp^2$ for various interaction strengths ζ (top axis) and corresponding scattering lengths a (bottom axis) at (a) 80 ms, (b) 120 ms, (c) 160 ms, and (d) 200 ms. Blue circles are averaged data over multiple shots with the same averaging and error bar calculation for Fig. 2. Bright red curves are predictions with the quasi-classical spin evolution model, and the pink bands correspond to a 2% standard deviation in cloud size σ_{F_x} .

spin-dependent energy states [18]. Further, the scattering length can be controlled with high spatial and temporal precision with an optical control technique [22]. Therefore, these energy-resolved probes can be exploited in broad studies of macroscopic out-of-equilibrium dynamics and critical dynamics across quantum phase transitions in quantum simulators.

We thank Ilya Arakelyan for helpful discussions. Primary support for this research is provided by the Air Force Office of Scientific Research (Grant No. FA9550-22-1-0329). Additional support is provided by the National Science Foundation (Grants No. PHY-2006234 and No. PHY-2307107).

-
- [1] A. Auerbach, *Interacting Electrons and Quantum Magnetism* (Springer, New York, 1994).
- [2] P. W. Anderson, Random-phase approximation in the theory of superconductivity, *Phys. Rev.* **112**, 1900 (1958).
- [3] J. Dukelsky, S. Pittel, and G. Sierra, *Colloquium*: Exactly solvable Richardson-Gaudin models for many-body quantum systems, *Rev. Mod. Phys.* **76**, 643 (2004).
- [4] P. Richerme, Z.-X. Gong, A. Lee, C. Senko, J. Smith, M. Foss-Feig, S. Michalakis, A. V. Gorshkov, and C. Monroe, Non-local propagation of correlations in quantum systems with long-range interactions, *Nature (London)* **511**, 198 (2014).
- [5] M. K. Joshi, A. Elben, B. Vermersch, T. Brydges, C. Maier, P. Zoller, R. Blatt, and C. F. Roos, Quantum information scrambling in a trapped-ion quantum simulator with tunable range interactions, *Phys. Rev. Lett.* **124**, 240505 (2020).
- [6] M. Gärttner, J. G. Bohnet, A. Safavi-Naini, M. L. Wall, J. J. Bollinger, and A. M. Rey, Measuring out-of-time-order correlations and multiple quantum spectra in a trapped-ion quantum magnet, *Nat. Phys.* **13**, 781 (2017).
- [7] L. W. Cheuk, M. A. Nichols, M. Okan, T. Gersdorf, V. V. Ramasesh, W. S. Bakr, T. Lompe, and M. W. Zwierlein, Quantum-gas microscope for fermionic atoms, *Phys. Rev. Lett.* **114**, 193001 (2015).
- [8] B. Swingle, G. Bentsen, M. Schleier-Smith, and P. Hayden, Measuring the scrambling of quantum information, *Phys. Rev. A* **94**, 040302(R) (2016).
- [9] K. R. A. Hazzard and B. Gadway, Synthetic dimensions, *Phys. Today* **76**(4), 62 (2023).
- [10] X. Du, Y. Zhang, J. Petricka, and J. E. Thomas, Controlling spin current in a trapped Fermi gas, *Phys. Rev. Lett.* **103**, 010401 (2009).
- [11] U. Ebling, A. Eckardt, and M. Lewenstein, Spin segregation via dynamically induced long-range interactions in a system of ultracold fermions, *Phys. Rev. A* **84**, 063607 (2011).
- [12] S. Pegahan, J. Kangara, I. Arakelyan, and J. E. Thomas, Spin-energy correlation in degenerate weakly interacting Fermi gases, *Phys. Rev. A* **99**, 063620 (2019).
- [13] F. Piéchon, J. N. Fuchs, and F. Laloë, Cumulative identical spin rotation effects in collisionless trapped atomic gases, *Phys. Rev. Lett.* **102**, 215301 (2009).
- [14] S. S. Natu and E. J. Mueller, Anomalous spin segregation in a weakly interacting two-component Fermi gas, *Phys. Rev. A* **79**, 051601(R) (2009).
- [15] C. Deutsch, F. Ramirez-Martinez, C. Lacroûte, F. Reinhard, T. Schneider, J. N. Fuchs, F. Piéchon, F. Laloë, J. Reichel, and P. Rosenbusch, Spin self-rephasing and very long coherence times in a trapped atomic ensemble, *Phys. Rev. Lett.* **105**, 020401 (2010).
- [16] S. Smale, P. He, B. A. Olsen, K. G. Jackson, H. Sharum, S. Trotzky, J. Marino, A. M. Rey, and J. H. Thywissen, Observation of a transition between dynamical phases in a quantum degenerate Fermi gas, *Sci. Adv.* **5**, eaax1568 (2019).
- [17] A. P. Koller, M. L. Wall, J. Munding, and A. M. Rey, Dynamics of interacting fermions in spin-dependent potentials, *Phys. Rev. Lett.* **117**, 195302 (2016).
- [18] M. L. Wall, Simulating fermions in spin-dependent potentials with spin models on an energy lattice, *Phys. Rev. A* **102**, 023329 (2020).
- [19] J. Huang, C. A. Royse, I. Arakelyan, and J. E. Thomas, Verifying a quasiclassical spin model of perturbed quantum rewinding in a Fermi gas, *Phys. Rev. A* **108**, L041304 (2023).
- [20] See Supplemental Material at <http://link.aps.org/supplemental/10.1103/PhysRevA.109.L041301> for a description of the experimental and data analysis details.
- [21] G. Pretzier, A new method for numerical Abel-inversion, *Zeitschrift für Naturforschung A* **46**, 639 (1991).
- [22] A. Jagannathan, N. Arunkumar, J. A. Joseph, and J. E. Thomas, Optical control of magnetic Feshbach resonances by closed-channel electromagnetically induced transparency, *Phys. Rev. Lett.* **116**, 075301 (2016).